Experimental Mechanics (2007) 47: 171–183
DOI 10.1007/s11340-006-0631-z

Capillary Adhesion Between Elastically Hard Rough Surfaces

M.P. de Boer

Received: 1 February 2006 / Accepted: 30 October 2006 / Published online: 10 January 2007

Abstract The adhesion versus vapor pressure (p/p_s) trend between two elastically hard rough surfaces is modeled and compared with experimental results. The experimental samples were hydrophilic surface-micromachined cantilevers, in which the nanometer-scale surface roughness is on the order of the Kelvin radius. The experimental results indicated that adhesion increases exponentially from p/p_s=0.3 to 0.95, with values from 1 mJ/m^2 to 50 mJ/m^2. Using the Kelvin equation to determine the force-displacement curves, the mechanics of a wetted rough interface are treated in two ways. First, the characteristics of a surface with rigid asperities of uniform height are derived. At low p/p_s, menisci surrounding individual asperities do not interact. Beyond a transition value, $[p/p_s]_{tr}$, a given meniscus grows beyond the asperity it is associated with, and liquid fills the interface. Capillary adhesion in each realm is found according to the integrated work of adhesion. Second, a more general approach allowing an arbitrary height distribution of Hertzian asperities subject to capillary forces is justified and developed. To compare with experimental results, a Gaussian height distribution is first assumed but significantly underestimates the measured adhesion. This is because equilibrium is found far into the Gaussian tail, where asperities likely do not exist. It is shown that by bounding the tail to more likely limits, the measured adhesion trend is more closely followed but is still not satisfactorily matched by the model. The uniform summit height model fits the data very well with a single free parameter. These results can be rationalized if the upper and lower surfaces are geometrically correlated.

Keywords Adhesion · Roughness · Capillarity · Contact mechanics · Elasticity · Plasticity · Vapor partial pressure · Relative humidity

M.P. de Boer (✉)
MEMS Devices and Reliability Physics Department,
Sandia National Laboratories,
Albuquerque, NM 87185, USA
e-mail: mpdebo@sandia.gov

Introduction

Liquids can penetrate porous media, greatly affecting the mechanical properties of dry solids. Resulting capillary forces are important in granular materials [1, 2], soil [3] and concrete [4] mechanics. Capillary forces are also important at technological interfaces such as in the head/disk system [5] and in microelectromechanical systems (MEMS) [6, 7]. The surface roughness of technologically fabricated films, frequently deposited by vapor deposition methods on smooth substrates, is often only several nanometers root mean square (rms). The Kelvin radius r_K, which is the radius of curvature of a liquid meniscus in equilibrium with a vapor of partial pressure p/p_s [8], is also on the order of nanometers for $0.3<p/p_s<0.95$. Therefore, a strong interaction between capillary adhesion and p/p_s for technologically fabricated surfaces can be expected.

Various theories for the adhesion *force* per unit area between nominally flat wetted interfaces have been proposed [9, 10]. The measured normal force to separate two nominally parallel surfaces inevitably reflects stress concentrators at which cracks initiate, and their geometry can vary significantly from one sample to the next. Hence, for the separation of nominally flat samples, it is difficult to compare

experiment to theory from a force per unit area criterion. On the other hand, the work or *energy* per unit area to separate the surfaces, Γ, can be accurately measured and within the framework of fracture mechanics [11]. Independently, Γ can be calculated as

$$\Gamma = \int_{d_{eq}}^{\infty} P(\delta)\mathrm{d}\delta. \quad (1)$$

Here P is the net attractive pressure, δ is the interface separation and d_{eq} is the equilibrium separation in the absence of external forces. Fracture mechanics test specimens based on a cantilever geometry can be manufactured by surface micromachining methods to measure Γ, and measurements from 1 μJ/m^2 to 100 mJ/m^2 can be accurately made with a single sample [12–14]. Furthermore, nanometer-scale surface topographic maps can be made. Hence, compliant surface-micromachined cantilevers offer an excellent platform for contributing to our understanding of capillary adhesion energies at rough interfaces.

Here, we shall examine experimental results on adhesion versus p/p_s, previously reported in a conference paper [15]. Models for the work of adhesion versus p/p_s are then derived. First, a surface that assumes uniform asperity heights is analyzed. This is extended to the more general case of an arbitrary height distribution of asperities. Finally, we shall compare model predictions to experimental results.

Experimental

The sample fabrication, the experimental apparatus and the experimental results, as previously reported [15], are described in this section. Further details describing the crack healing rates and the surface topography measurements are also given. The test sample used to measure adhesion was an array of polycrystalline silicon (polysilicon) cantilevers fabricated by surface micromachining. The process consisted of repeated deposition, lithographic definition, annealing and etching of polysilicon and sacrificial silicon oxide layers [16]. At the end of the fabrication process, the sacrificial oxide layers were dissolved in HF:HCl solution and the parts were cleaned according to the RCA-1 procedure [17]. If dried in air, water pulls compliant structures into contact with the substrate by capillary action, resulting in permanent adhesion (also known as stiction) [6, 7]. Therefore, critical-point drying, using supercritical carbon dioxide as the working fluid, was used to obtain free-standing cantilevers free [18]. Twenty cantilevers, of lengths 1,050 μm≤L≤2,000 μm in 50 μm increments, were on the same test piece. The height of the step-up support post was h=1.8 μm, the cantilever width was w=20 μm and the cantilever thickness was t=2.5 μm.

To render the surface hydrophilic while minimizing surface charging, the cantilevers were exposed to a downstream oxygen plasma. The contact angle of the polysilicon surfaces with water after this treatment was 0°. The samples were then placed in an environmental chamber where p/p_s could be controlled from 0.01 to 1 (corresponding to a relative humidity range from 1 to 100%) by combining dry and wet nitrogen. This chamber also allowed viewing of the samples with optical interferometry, from which out-of-plane deflections are measured with a resolution of 10 nm/pixel.

The cantilevers were placed in the chamber in dry nitrogen ambient (p/p_s=0.01) for 16 h to minimize adsorbed water. As seen in Fig. 1, they were brought into contact with the landing pad using an electric potential of 150 V applied to the actuation pad (of length a=50 μm). The cantilever and the landing pad were electrically grounded so that their interaction was adhesive only [14, 19]. The voltage was reduced to 0 V, and the cantilevers remained adhered to the polysilicon substrate. Most cantilevers remained adhered in the "S-shape" [12], in which the cantilever is parallel to the substrate beyond the crack tip at s.

The adhesion energy per unit area Γ of a given cantilever was calculated according to [12]

$$\Gamma = \frac{3}{2}E\frac{h^2t^3}{s^4}. \quad (2)$$

The Young's Modulus E of the polysilicon is 164 GPa [20] and Poisson's ratio for silicon is ν=0.22. The crack length is determined by matching the deflection data υ to a model curve [12]. With crack length s ranging initially from 600 μm to 850 μm in dry nitrogen, corresponding values of adhesion were Γ=0.068−0.017 mJ/m^2, respectively.

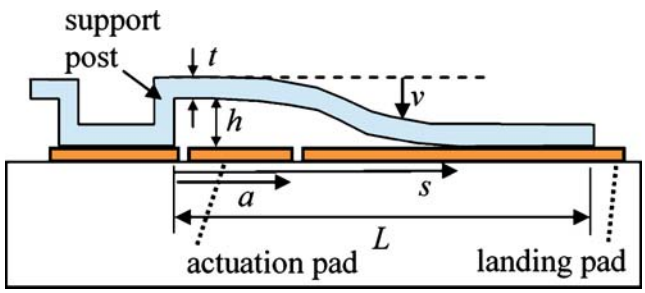

Fig. 1 Schematic cross-section of adhered microcantilever configured in the *S* shape

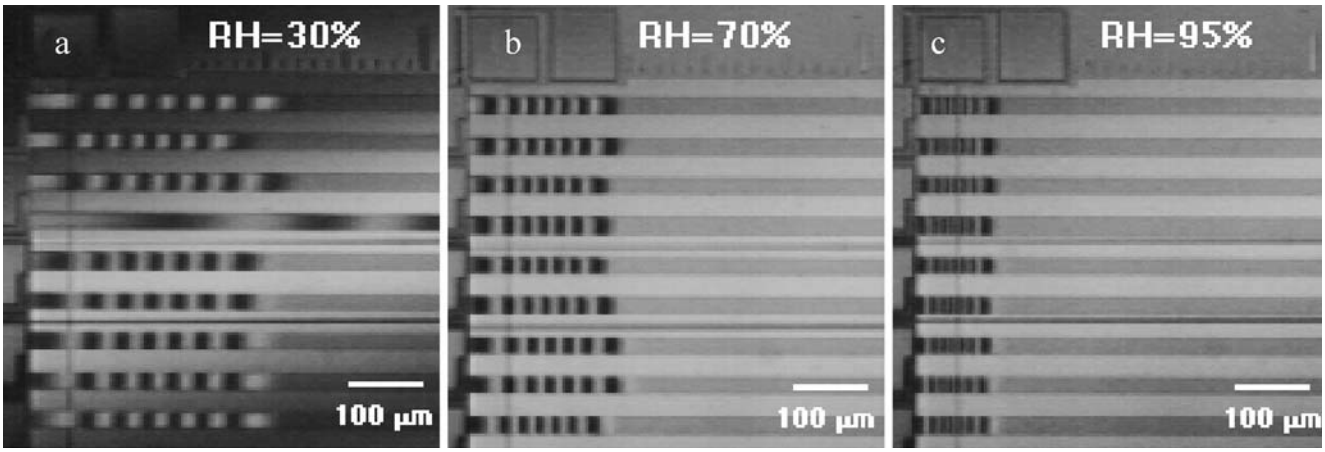

Fig. 2 Interferograms of crack length s vs. RH (p/p_s) after 40 h exposure

The value of p/p_s was increased to 0.3, and the crack lengths spontaneously decreased. An equilibrium value for crack length, as monitored by interferograms taken every 30 min, was achieved gradually. The average crack length decreased from s_{avg}~700 μm initially to s_{avg}~550 μm after 1.5 h, to s_{avg}~400 μm after 5 h, and to s_{avg}~375 μm after 10 h. At this time, the minimum crack length was s_{min}~350 μm (Γ= 0.6 mJ/m^2), and did not decrease further. Cantilevers of lengths 1,050 μm≤L≤1,200 μm, originally in the "arc-shape" (i.e., contacting only at the end), reconfigured into the S-shape and also decreased to s~350 μm over the next 30 h.

After a 40-h exposure to p/p_s=0.3, only one cantilever remained adhered in the arc-shape configuration. This was the fourth cantilever from the top in Fig. 2(a), and its length was L=1,200 μm. The value of p/p_s was then successively increased to 0.45, 0.55, 0.7 and 0.95.

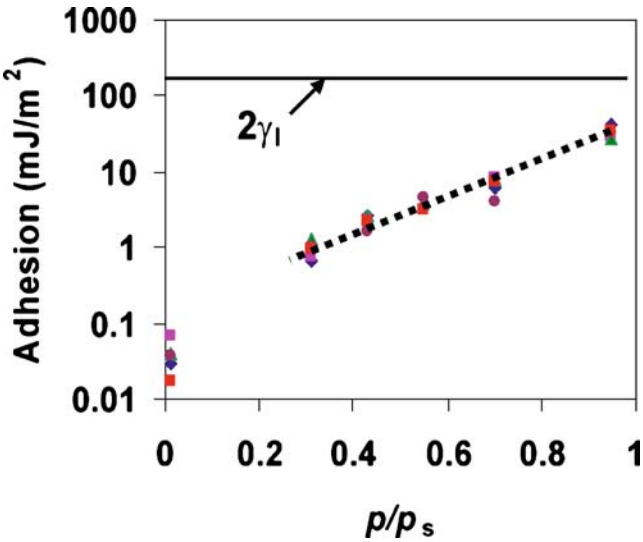

Fig. 3 Adhesion data with least squares fit to data over the range 0.3<p/p_s<0.95 (r^2=0.96). Also indicated are the upper limit due to capillary adhesion ($2\gamma_l$) and the adhesion at p/p_s≈0.01

At each RH value, crack length steadily decreased until no decrease was observed after approximately 16 h. The p/p_s level was maintained from 24 to 40 h before increasing to the next level. Between 1 and 1.5 h at p/p_s=0.45, the L=1,200 μm cantilever also assumed the S-shape, and had a crack length identical to other cantilevers within 4 h. At p/p_s=0.95, equilibrium was attained within 1 h. As seen in Fig. 2(b) at p/p_s=0.7 and Fig. 2(c) at p/p_s=0.95, the equilibrium crack lengths were 200 μm (Γ=6 mJ/m^2) and 130 μm (Γ=33 mJ/m^2), respectively. The adhesion for each of five cantilevers at the five different RH values ranging from 0.01≤p/p_s≤0.95, and is plotted in Fig. 3.

Contact mode atomic force microscopy was used to characterize the surface topography of the upper and lower surfaces. Representative images are shown in Figs. 4(a) and (b). The surface roughness of the top of the landing pad is 1.62 nm root means square (rms), while the roughness of the bottom of the cantilever is 2.31 nm rms. The asperity radius of curvature R was estimated by fitting to linescans of individual asperities. In Fig. 4(c), for example, a typical value of R=500 nm is seen.

Model

At p/p_s=0.01, the average value of Γ is 0.03 mJ/m^2 while the equivalent surface roughness is 2.8 nm. This value is larger than Γ=0.008 mJ/m^2, which was measured when the equivalent surface roughness was 3.7 nm [21]. In that case, the adhesion was modeled well by accounting for the van der Waals forces of the contacting and non-contacting areas. Given that the current roughness is smaller, the value of 0.03 mJ/m^2 is consistent with dry adhesion mechanisms. However, over the range of 0.3≤p/p_s≤0.95, capillary bridges can

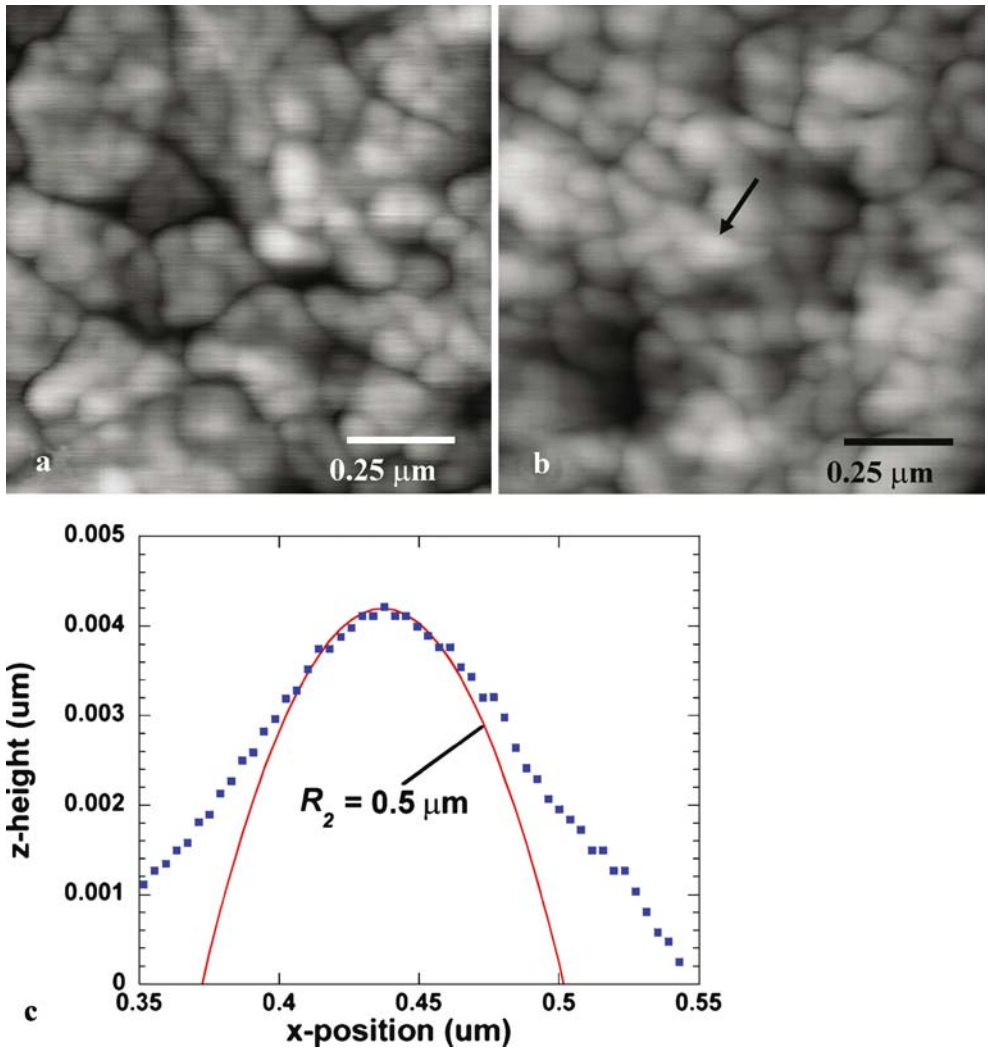

Fig. 4 Atomic force micrographs showing the topography of the two surfaces (1 μm field of view, 10 nm *z*-range) (**a**) *top of landing pad* (1.62 nm rms), (**b**) *bottom of cantilever* (2.31 nm rms) (**c**) example linescan and curve fit across the asperity *indicated by the arrow* in (**b**)

nucleate between the surfaces. The adhesion is then much higher, reflecting the much longer range of capillary forces. In the remainder of this paper, two models incorporating these forces will be developed and compared with the data.

A complete description of the interactive phenomena that contribute to the work of adhesion at a rough, wet interface is complex. The models here address the basic physical mechanisms of capillary forces, elastic repulsion between contacting asperities and non-interacting as well as interacting menisci. In the first model ("Constitutive Laws for Single Asperity and Parallel Plates" and "Case of Uniform Asperity Heights"), it is assumed that all asperities are at the same height and are initially in contact with the substrate. At sufficiently low values of p/p_s, menisci condense around the asperities but do not interact, and therefore a single-asperity constitutive law applies. At high p/p_s, menisci merge, and therefore the initial capillary force is governed by a flat plate solution. These two realms are described and linked in "Case of Uniform Asperity Heights". In the second model ("Case of Asperity Height Distribution"), a more general treatment allowing a distribution of asperity heights and elastic repulsion is developed.

Constitutive Laws for Single Asperity and Parallel Plates

The geometry for a single asperity is shown in Fig. 5(a). A meniscus of radius r_K, corresponding to the Kelvin radius, bridges the flat surface and the sphere of radius R. The contact angle between the meniscus and the surfaces is θ (fully wetting corresponds to θ=0°). The Kelvin radius depends on surface tension γ_l of the condensing liquid, the temperature, the molar volume V, and the partial pressure of the vapor. Under standard conditions for water (V=0.018 l/mol, γ_l=

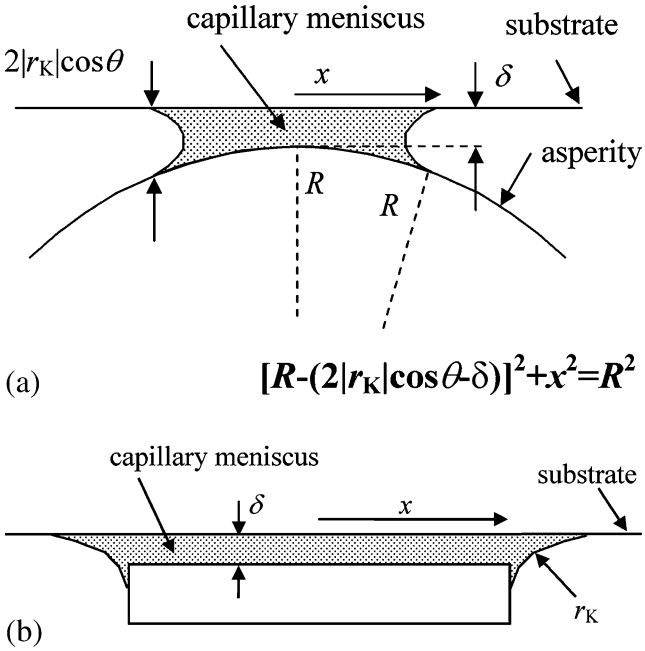

Fig. 5 A capillary of radius r_K bridging (**a**) a *sphere* on a substrate (**b**) two *parallel* flat disks

0.073 N/m, R=0.082 l atm/(mol °K), T=300 °K, 1 atm=1.013•10^5 N/m^2),

$$r_K = \frac{\gamma_l V}{RT \ln(p/p_s)} = \frac{0.53}{\ln(p/p_s)} \quad \text{nm.} \tag{3}$$

The Kelvin radius is negative for $0<p/p_s<1$. In turn, significant negative (tensile) pressures exist in the liquid according to the Laplace equation,

$$\Delta P = \gamma_l / r_k. \tag{4}$$

It is this attractive tensile pressure that gives rise to the very strong capillary forces and large adhesion in micron-scale structures. Liquids are metastable in tension and are susceptible to spinodal decomposition. However, in the absence of cavitation, very high negative pressures can be sustained by the van der Waals or hydrogen bonding between adjacent liquid molecules. Indeed, pressures of −140 MPa have been measured for bulk water [22], in good agreement with vapor nucleation theory [23]. Using equations (3) and (4), −140 MPa places a lower bound on p/p_s at 0.37. However, the critical vapor nucleus radius at a given pressure, as calculated from the nucleation theory, is larger than the Kelvin radius. Therefore, the lower bound value may be smaller. However, as $|r_K|$ decreases, it reaches the size of individual molecules (a water molecule is ~0.3 nm in diameter [8]) and continuum theory must reach a limit.

From the geometry represented in Fig. 5(a), using equation (4), and with the approximation $R \gg |r_K| \cos\theta$, the capillary force at fixed Kelvin radius between the two bodies at separation δ is

$$F_c = (\delta) = 4\pi R\gamma_l \cos\theta \left[1 - \frac{\delta}{2|r_K|\cos\theta}\right] \tag{5}$$

for $\delta \leq 2|r_K|\cos\theta$ [24]. Attractive forces are taken to be positive. It assumed here that $\gamma_l \cos\theta \gg \gamma_{sl}$ (as is often the case (Chapter 15 of [8]), where γ_{sl} is the liquid–solid adhesion energy.

Surface force apparatus measurements validate an adhesion force of $4\pi R\gamma_l \cos\theta$ (at δ=0) for crossed cylinders of mica in water vapor for p/p_s above 0.7 [25]. However, the adhesion force decreased to a limiting value of $3\pi R\gamma_l \cos\theta$ for p/p_s approaching zero. Fogden and White [26] developed a dimensionless parameter

$$k = \left(\frac{3}{4}\sqrt{\frac{\pi}{2}}\right)\left(\frac{K}{\gamma_l}\right)\frac{[|r_k|(1 - D_o/2|r_k|)]^{3/2}}{\sqrt{R}} \tag{6}$$

where $K = (4/3)\left(E/\left\lfloor 2(1-\upsilon^2)\right\rfloor\right)$, υ is Poisson's ratio and D_o atomic spacing when the surfaces are in contact. The parameter k is related to the inverse of the Tabor parameter [27], which describes the transition from the Johnson–Kendall–Roberts (JKR) [28] regime to the Derjaguin–Muller–Toporov (DMT) [29] regime. Small k ($\ll$1) corresponds to large spheres at low vapor pressures. This extreme is JKR-like and the coefficient in equation (5) changes from 4 to 3. Large k ($\gg$1) applies to small hard spheres at high vapor pressures and this extreme is DMT-like. The coefficient remains as in equation (5) and the sphere deformations are Hertzian.

Fogden and White's paper clarifies that the mica in water vapor experiment [25] does not necessarily bound the lower limit of equation (3) with respect to p/p_s because k=1 at p/p_s=0.7. In a recent report, capillary forces at p/p_s=0.15 were detected for silicon tips with R ranging from 50 to 400 nm, and capillarity theory was used to accurately model the force-displacement curves [30]. In the current experiment, R=260 nm (see below) and K=115 GPa. Then k=3,115 at p/p_s=0.95 and k=24 at p/p_s=0.3, i.e., $k \gg 1$. Therefore, equation (5) applies to the present experiment, and the deformations of the sphere can be treated as Hertzian.

In the context of Hertz theory, equation (5) is also a good approximation of the capillary force for $\delta<0$ if $R \gg |r_K|$ and the range $0.3 \leq p/p_s \leq 0.95$ is used. Using the exact Hertzian deformation profile calculated from equation 3.42(a) in [31], the error incurred by this

approximation can be calculated. Using a force of 1 μN (the average force on a contacting asperity as will be seen below) and R=260 nm, it is found that equation (5) overestimates the exact capillary force by 0.2% at p/p_s=0.95 and by 10.0% at p/p_s=0.3. In view of simplicity, equation (5) will be used in "Case of Asperity Height Distribution" instead of an exact formulation.

It should be noted that the authors in [30] modeled their data with the constant volume limit. However, they first allowed their tips to come into contact with the substrate and equilibrate before measuring pull-off curves. Considering that as described in "Experimental," the cracks healed spontaneously, the present experiment measures the integrated force-displacement law of asperities approaching each other. The constant pressure constitutive law [(i.e., equation (5)] shall be used here, which corresponds to thermodynamic equilibrium.

Assuming $\delta \geq 0$ and integrating over this range according to equation (1), the work of adhesion for the asperity geometry is

$$W_{\mathrm{asp}}(\delta) = \int_{\delta}^{2r_{\mathrm{K}}\cos\theta} F_{\mathrm{c}}(\delta')\mathrm{d}\delta' = 4\pi R\gamma_1 \cos\theta |r_{\mathrm{K}}| \cos\theta \left(1 - \frac{\delta}{2|r_{\mathrm{K}}|\cos\theta}\right)^2. \tag{7}$$

For an asperity initially contacting the substrate (δ=0), the work of adhesion is $W(0) = 4\pi R\gamma_1 \cos\theta |r_{\mathrm{K}}| \cos\theta$.

Consider now the work of adhesion between two parallel plates subject to capillary condensation. With a disc of radius $x_{\mathrm{d}} \gg |r_{\mathrm{K}}|$ as in Fig. 5(b), the force is independent of the separation, such that

$$F_{\mathrm{c}} = \pi x_{\mathrm{d}}^2 \frac{\gamma_1}{|r_{\mathrm{K}}|}. \tag{8}$$

In this case, capillary condensation must take place as the plates are separated under equilibrium conditions. The force is independent of the contact angle because the force is applied purely against the liquid surface tension. The work of adhesion of two plates initially separated by δ is

$$W \approx \int_{\delta}^{2|r_{\mathrm{K}}|\cos\theta} F_{\mathrm{c}}(\delta')\mathrm{d}\delta' = 2\gamma_1 \cos\theta \pi x_{\mathrm{d}}^2 \left(1 - \frac{\delta}{2|r_{\mathrm{K}}|\cos\theta}\right). \tag{9}$$

If δ is taken to be zero, then $W(0) = 2\pi x_{\mathrm{d}}^2 \gamma_1 \cos\theta$, and the work of adhesion per unit area is $2\gamma_1 \cos\theta$.

Case of Uniform Asperity Heights

The work of adhesion of spherically-capped asperities, of radius R and areal density n_{asp}, all of which are at the same height as in Fig. 6(a), is considered in this section. A surface with uniform asperity heights is much stiffer than one with a distribution of heights. Because capillary attraction dominates the integrated force-displacement curve, the elasticity of the asperities is neglected.

In Fig. 6(a), the largest separation between the substrate and the rough surface, $z_{\max}$, is related by geometry to n_{asp}. For a square array of asperities

$$z_{\max} = \frac{1}{8Rn_{\mathrm{asp}}}. \tag{10}$$

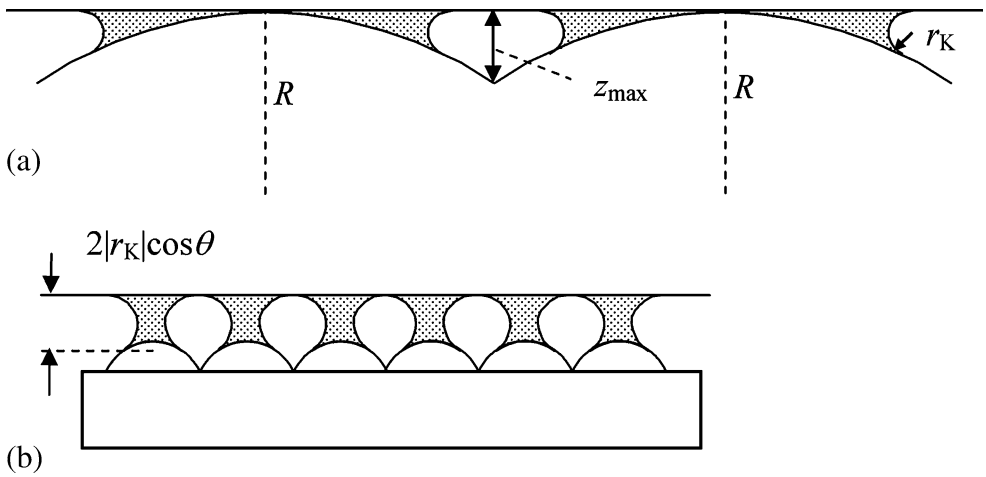

Fig. 6 Array of *spheres* with areal density $n_{\mathrm{asp}}=1/(8Rz_{\max})$ contacting a plane, with liquid bridges of radius r_{K} providing adhesive energy. (**a**) undersaturated asperities (**b**) initially saturated asperities, with the surfaces partially separated

Using equation (7) with δ=0, the adhesion for an under-saturated interface ($2|r_K|\cos\theta<z_{max}$) is

$$\Gamma = n_{asp}\, W_{asp} = 4\pi n_{asp} R|r_k|\ \gamma_1\ \cos\theta^2. \tag{11}$$

Using equations (3) and (10), this is recast in terms of p/p_s as

$$\Gamma = \left(\frac{\pi}{2}\right)\left(\frac{0.53\ \text{nm}}{z_{max}}\right)\frac{\gamma_1 \cos^2\theta}{|\ln(p/p_s)|} \tag{12}$$

When asperities begin to merge ($2|r_K|\cos\theta>z_{max}$), the geometry becomes that of a flat plate bridged by liquid. The work of adhesion is the work to separate the plane of the flat plate to a separation of $2|r_K|\cos\theta - z_{max}$, plus the remaining work to separate the menisci from the protruding asperities [Fig. 6(b)],

$$\Gamma \approx \left(\frac{\gamma_1}{|r_K|}\right)(2|r_K|\cos\theta - z_{max}) + n_{asp}\int_{2|r_K|\cos\theta - z_{max}}^{2|r_K|\cos\theta} F(\delta')\mathrm{d}\delta'. \tag{13}$$

This expression is approximate because it ignores the details of meniscus separation as the transition from the saturated to the under-saturated interface occurs. Accurate treatment of this issue requires a full three-dimensional formulation. Given that this meniscus separation occurs only over a small range of δ, ignoring this effect induces inaccuracy only over a small range of p/p_s. Proceeding with equations (5) and (10), for an initially saturated interface

$$\Gamma \approx 2\gamma_1\cos\theta\left(1 - \frac{z_{max}}{2|r_K|\cos\theta}\right) + \frac{\pi}{8}\gamma_1\frac{z_{max}}{|r_K|}. \tag{14a}$$

Setting $z_{max}=\varepsilon R$ where $\varepsilon \ll 1$, and recasting in terms of p/p_s,

$$\Gamma \approx 2\gamma_1\cos\theta\left(1 - \frac{\varepsilon R|\ln(p/p_s)|}{2(0.53\ \text{nm})\cos\theta}\right) + \frac{\pi}{8}\gamma_1\frac{\varepsilon R|\ln(p/p_s)|}{0.53\ \text{nm}} \tag{14b}$$

To illustrate, assume ε=0.03, γ_l=73 mJ/m^2 and θ=0°. Equations (11) and (14b) are then plotted versus p/p_s in Fig. 7. The transition from equation (11) to equation (14b) is defined by the condition $2|r_K|\cos\theta=z_{max}$, or equivalently

$$[p/p_s]_{tr} = \exp\left(-\frac{2(0.53\ \text{nm})\cos\theta}{\varepsilon R}\right), \tag{15}$$

is indicated by the asterisk. Strictly, Γ reaches $2\gamma_1\cos\theta$ only at p/p_s=1. Also shown are the adhesion values if only van der Waals forces are considered according to a DMT model.

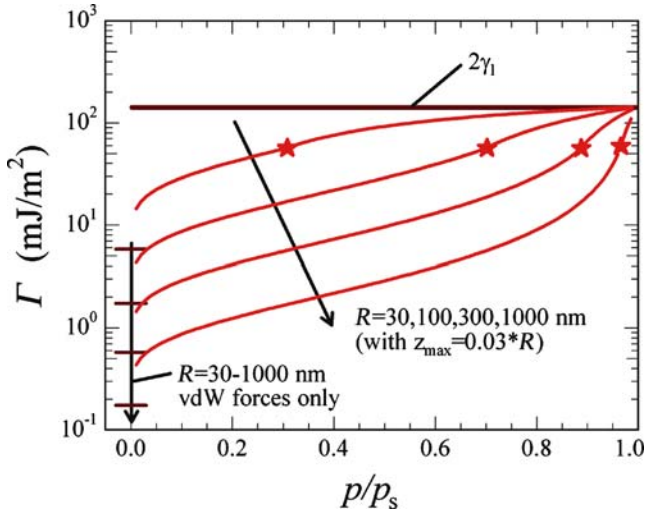

Fig. 7 Γ vs p/p_s (with z_{max}=0.03R, γ_l=73 mJ/m^2 and θ=0°). The * marks the delineation between equations (11) and (14b). Also shown are the adhesion values if only van der Waals forces are considered according to a DMT model

The trend in Fig. 7 is similar to the experimental trend, as will be seen in "Model Evaluations." However, the asperities in Fig. 3 are not all at the same height. This observation motivates the development of a model that takes into account a distribution of asperity heights.

Case of Asperity Height Distribution

When there is a distribution of asperity heights it is no longer reasonable to neglect their elastic deformation. Here, the applied pressure is due to the attractive capillary forces. Greenwood and Williamson [32, 33] (henceforth referred to as GW) determined the elastic contact mechanics between rough surfaces under the assumptions of non-interacting asperities of radius R and of density n_{asp}. Surface models with a Gaussian asperity height distribution are widely used in the literature. Fuller and Tabor extended the GW model to calculate adhesion between two rough surfaces assuming adhesive tractions occur only in the area of contact [34]. Maugis reviewed these models and showed how adhesion due to van der Waals forces just outside the contact area could be calculated [35]. The model developed in this section extends the GW model to the case of capillary forces. In "Model Evaluations" the asperity height distribution function will be considered in view of the surface topography measurements.

The model geometry is represented in Fig. 8, where the mean asperity height is at z=0 and the distance

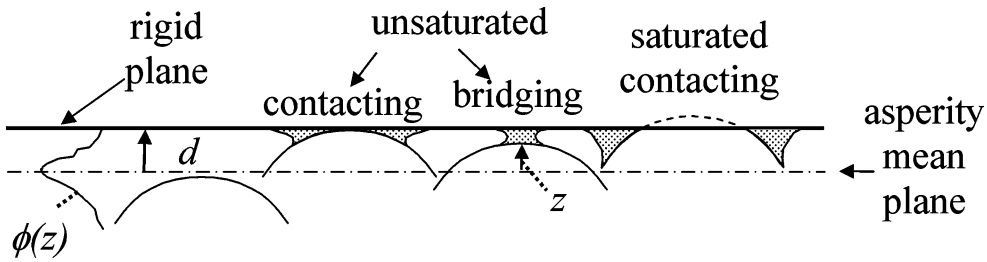

Fig. 8 Asperities of height distribution $\phi(z)$ with mean plane indicated. The distance from the asperity mean plane to a summit is z. Both contacting ($d-z\leq 0$) and non-contacting asperities bridged by menisici ($d - z < 2|r_K|\cos\theta$) are considered to contribute to the capillary force

between the asperity mean plane and the rigid surface is d. Note that the quantity $(d-z)$ is equivalent to δ in Fig. 5(a). The asperity peak heights are distributed as described by the function $\varphi(z)$, which is normalized according to

$$\int_{-\infty}^{\infty} \varphi(z)\mathrm{d}z = 1. \tag{16}$$

Here, z is the distance from the asperity mean plane to the summit peak. To obtain the expected value for a given property, $\varphi(z)$ is multiplied by the property and integrated over appropriate limits. Hence, the number of contacting asperities in contact per unit area is

$$n_c = n_{asp}\int_{d}^{\infty} \varphi(z)\mathrm{d}z, \tag{17a}$$

while the number of non-contacting asperities bridged by a liquid meniscus is

$$n_{nc} = n_{asp}\int_{d-2|r_K|\cos\theta}^{d} \varphi(z)\mathrm{d}z, \tag{17b}$$

The area associated with a given asperity is $1/n_{asp}$. Considering the geometry of Fig. 6(a), an asperity is saturated if

$$\pi x^2 \geq 1/n_{asp} \tag{18a}$$

Associating the quantity $2|r_K|\cos\theta-\delta$ in Fig. 5(a) with $\Delta_i = (z_i - d) + 2|r_K|\cos\theta$ for the ith asperity in Fig. 8, saturation occurs when

$$z_i \geq d + 1/\left(2\pi R\, n_{asp}\right) - 2|r_K|\cos\theta. \tag{18b}$$

Note that saturated asperities may or may not be in contact. Defining $d_{sat} = 2|r_K|\cos\theta - 1/\left(2\pi R\, n_{asp}\right)$, the number of saturated asperities per unit area is

$$n_{c,s} = n_{asp}\int_{d-d_{sat}}^{\infty} \varphi(z)\mathrm{d}z, \tag{19a}$$

while the number of unsaturated asperities per unit area is

$$n_{c,us} = n_{asp}\int_{d-2|r_K|\cos\theta}^{d-d_{sat}} \varphi(z)\mathrm{d}z, \tag{19b}$$

The capillary force on saturated asperities is

$$F_{c,s} = \frac{\gamma_l}{|r_K|}\frac{1}{n_{asp}} \tag{20a}$$

while the capillary force on unsaturated asperities is

$$F_{c,us} = 4\pi R\gamma_l\cos\theta\left(1 - \frac{d - z_i}{2|r_K|\cos\theta}\right). \tag{20b}$$

The attractive pressure due to saturated asperities is

$$P_{c,s} = \frac{\gamma_l}{|r_K|}\int_{d-d_{sat}}^{\infty} \varphi(z)\mathrm{d}z \tag{21a}$$

Applying equation (5), the attractive pressure from unsaturated asperities is

$$P_{c,us} = 4\pi\gamma\cos\theta\, R n_{asp}\int_{d-2|r_K|\cos\theta}^{d-d_{sat}} \left(1 - \left(\frac{d - z}{2|r_K|\cos\theta}\right)\right)\varphi(z)\mathrm{d}z. \tag{21b}$$

The total attractive pressure is then

$$P_c = P_{c,s} + P_{c,us}, \tag{22}$$

From Hertzian mechanics (as justified in "Constitutive Laws for Single Asperity and Parallel Plates"), the elastic repulsion pressure is

$$P_r = n_{asp}\int_{d}^{\infty} KR^{1/2}(z - d)^{3/2}\varphi(z)\mathrm{d}z, \tag{23}$$

where $K = (2/3)\left(E/\left(1-\upsilon^2\right)\right)$ for two rough surfaces in contact. Force equilibrium occurs at a separation d_{eq} such that

$$P_c(d_{eq}) - P_r(d_{eq}) = 0 \tag{24}$$

Once d_{eq} is determined, the adhesion energy per unit area is found according to equation (1). Note that in this model, $[p/p_s]_{tr}$=1 provided that there is a non-zero probability of an asperity for all z<0.

Model Evaluations

For a Gaussian asperity height distribution, $\varphi(z)$ is

$$\varphi(z) = \frac{1}{\sigma_s\sqrt{2\pi}} \exp\left[-\frac{1}{2}\left(\frac{z}{\sigma_s}\right)^2\right], \tag{25}$$

where σ_s is the asperity height standard deviation. McCool [36] has summarized and contributed to the work of Nayak [37] and Longuet–Higgins [38] to show how topographic data can be converted into Gaussian asperity distribution data. That approach was applied to the topographic data from surfaces of Fig. 4 and the resulting input values, representing a conversion from two rough surfaces to an equivalent single rough surface against a rigid plane, are given in Table 1.

The value in Table 1 for R agrees well with curvature measurements made on actual asperities as shown in Fig. 4(c). A value of R_1=480±117 nm (one standard deviation, 18 measurements) was found on the surface of the landing pad, and R_2=540±109 nm (one standard deviation, 18 measurements) was found on the cantilevers. Then, from $R = (1/R_1 + 1/R_2)^{-1}$, R=254 nm. The relatively small standard deviations for R substantiate the assumption of constant R. The value of n_{asp} appears to be reasonable when comparing to Fig. 4. The assumption $R \gg r_K$ is also validated. The applicability of σ_s over the entire distribution range will be considered below.

Before evaluating the elastic model according to the Gaussian distribution assumption, the issue of asperity plasticity must be considered. GW have proposed a plasticity parameter

$$\Psi = \frac{E'}{H}\sqrt{\frac{\sigma_s}{R}}. \tag{26}$$

Here $E' = E/2\left(1-\upsilon^2\right)$ and H is the hardness. When Ψ<0.6 the deformation is elastic, while when Ψ>1, the deformation is predominantly plastic. With E'=86 GPa and H=11 GPa for polysilicon [39], σ_s=2.50 nm and R=260.5 nm, a value of Ψ=0.80 is found. Because there

Table 1 GW input values using McCool's method

Parameter	Value
R (nm)	260.5
σ_s (nm)	2.50
n_{asp} (per μm^2)	80.1
K (GPa)	115.4

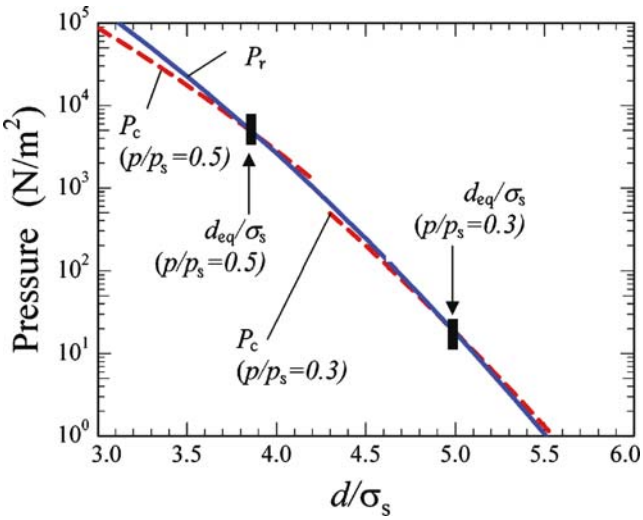

Fig. 9 Force versus separation trend at p/p_s=0.3 and p/p_s=0.5

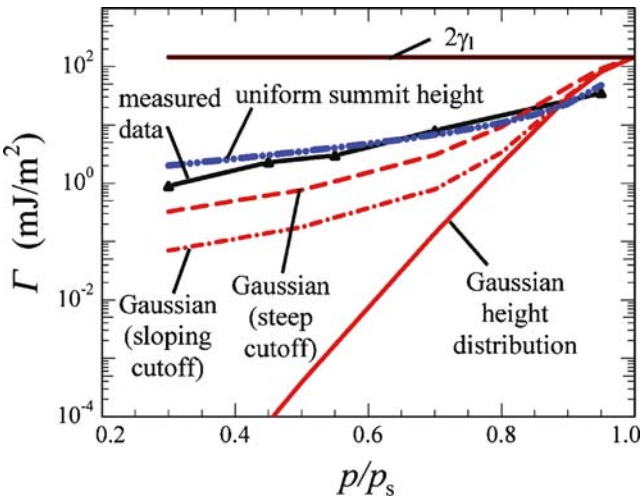

Fig. 10 Adhesion versus p/p_s trend for measured data and the model with Gaussian and Gaussian-cutoff distributions. Also equation (11), the uniform summit height model with free parameter n_{asp} is plotted (similar results are obtained with a steep Gaussian cutoff at d/σ_s=1.7). The results can be rationalized if there is a topographic correlation between the upper and lower surfaces (see text)

is a relatively small amount of plasticity, it is not necessary to apply the plasticity theory of rough contacts [40] here.

Using the values from Table 1, the dependencies of P_c and P_r on d are found from equations (22) and (23), respectively. In Fig. 9, these are plotted for p/p_s=0.3 and 0.5, and the equilibrium separations (F_a=F_r) are found at d_{eq}/σ_s=4.97 and 3.87, respectively. Applying equation (1), the predicted adhesion versus p/p_s trend is plotted in Fig. 10 (Gaussian height distribution), and it is seen that for p/p_s<0.9, the measured data are severely under-predicted. The average load for contact asperities is $P_r(d_{eq})/n_c(d_{eq}) \approx 1\mu N$. As discussed above, this leads to at most a 10% overestimate of the capillary forces, which does not explain the large underestimate of the model when compared with the experiment.

In Fig. 9, the force equilibrium occurs at large values of d_{eq}/σ_s. The question of whether Gaussian statistics apply to such large values bears scrutiny. That is, the model assumes that a very low probability event must occur. If the assumed asperities are not available, the surface separation will be smaller, and adhesion will be larger. To investigate whether this low probability event actually occurs, an algorithm that searches for asperities [41] was applied to the AFM data in the 4×4 um^2 area (256×256 pixels). To make the transformation to two rough surfaces against a rigid plane, the AFM data from the opposing surfaces was added together. Using a neighborhood search factor of 4 pixels, a typical distribution of asperity heights is shown in Fig. 11. Here, it is seen that the previous value of σ_s is reasonable (σ_s=2.5 in Table 1 and σ_s=2.4 in Fig. 10). Furthermore, the Gaussian function fits the data out to approximately 2.7σ_s.

For d/σ_s>3, there is uncertainty as to the applicability of the Gaussian probability function. First, the area associated with such large values is much larger than the area than the experiment measures. For example, with d/σ_s=4.97, equation (19a) gives n_c=2.3•10^{-5}/μm^2, meaning that there is one contacting asperity in an area of 43,000 μm^2. Considering that w=20 μm, the corresponding adhesion length would be 2,200 μm. The cantilever beam geometry measures adhesion locally over a length of about 5t [12], which corresponds to an area of 5wt=125 μm^2. To ensure that at least one contacting asperity in this region, $d/\sigma_s \leq 3.72$ is required. Second, the highest asperities will be deformed plastically because of large local normal tractions as the crack tip passes over a given area. The calculation in the Appendix show that this will reduce the height of very high asperities by approximately 1.3 nm, or 0.5σ_s.

A detailed calculation of these effects is beyond the scope of this work and would involve considering the areal statistics, characterization of the skew and kurtosis of the distribution [42], and the elastic-plastic unloading of the rough surfaces [43]. To bound the likely effects, two tail distributions are considered as in Fig. 11. The first is the "sloping cutoff," which likely overestimates the true distribution of asperities in the tail region, and drops to 0 at d/σ_s=3. This distribution was normalized according to equation (16), and the predicted adhesion is shown in Fig. 10. While it still underestimates the measured adhesion, it is within a factor of 12 at the low p/p_s values. The second is the "steep cutoff," which likely underestimates the true asperity distribution. The corresponding adhesion is shown in Fig. 10 and shows that the trend is closer to the measured data, but still underestimates it by a factor of 4 at low p/p_s. Empirically, a sharp cutoff at d/σ_s=1.7 predicts the measured data quite well, but cannot be justified by the considerations mentioned. It can be concluded from these calculations that the adhesion is very sensitive to the details of the distribution tail, but that some important detail of the surface topography is not captured even when reasonable bounds are placed on it.

Let us now consider the simpler model developed in "Case of Uniform Asperity Heights." Using R=260.5 nm and allowing n_{asp} as a single free parameter, equation (11) compares favorably with respect to the GW-type models as seen in Fig. 10. A value of n_{asp}=20/μm^2 was used, which is one quarter of the measured value of 80/μm^2. Also, from equation (10), z_{max}=25 nm. Because εR=z_{max}, from equation (15) $[p/p_s]_{tr}$=0.96.

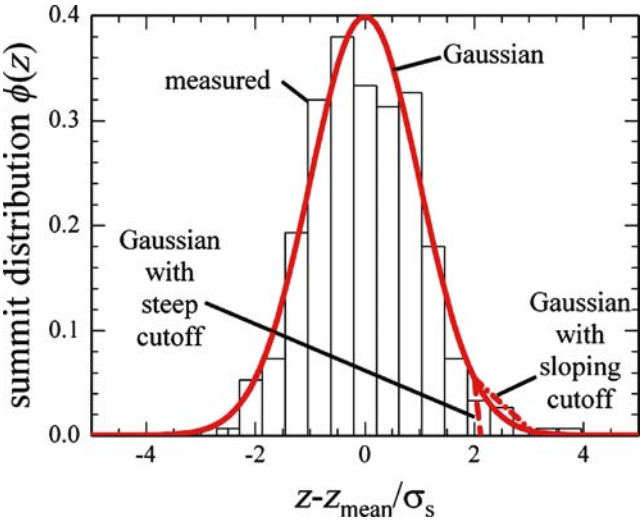

Fig. 11 The asperity distribution as determined from a nearest-neighbor algorithm and compared to a Gaussian distribution with σ_s=2.4 nm. The plot also shows the sloping and steep cutoff distributions assumed in Fig. 10

Hence only equation (11) need be applied over the range of the data. Because this model incorporates no asperity distribution but does fit the data well, the idea that there is a cutoff in the tail is further supported.

One implicit assumption in topography models is there is no surface correlation. At larger surface roughness values correlation of the upper and lower polysilicon layers has been observed [21, 44], and is due to a degree of conformation of the sacrificial oxide layer to the underlying substrate. Surface correlation would explain how much larger real contact areas than those predicted by GW-like models could exist, and why the very simple model of "Case of Uniform Asperity Heights" works relatively well. It might also justify a cutoff value at d/σ_s=1.7, which fits the data as well as the simple model, i.e., equation (11) with n_{asp}=20/μm^2. According to this idea, the highest asperities on the lower surface are aligned with pits on the upper surface, and therefore the average surface separation is less than the calculated value. Proving that this is indeed the key issue will involve detailed AFM measurements of locally aligned counterfaces.

Finally, it should be noted that the experiment described in "Experimental" was previously modeled [45]. The authors calculated a plasticity parameter of Ψ=14 rather than 0.8 as found here. Plasticity then gave rise to a hard wall in the tail of the distribution. The model, which used a step function constitutive law rather than an integrated force-displacement constitutive law [i.e., equations (7) and (9)], found that adhesion versus p/p_s increased beyond the measured value at p/p_s=0.4. However, the present work, which analyzed these particular surfaces in greater detail, does not support the contention that a hard wall forms due to plastic deformation.

Summary and Concluding Remarks

The adhesion trend of two contacting rough surfaces versus p/p_s has been reported. To gain insight into the results, two models were developed. The first model accounts for the roughness of the surface, but not the distribution of asperity heights. The second is an extension of the Greenwood–Williamson (GW) model of rough surfaces. Based on Fogden and White's k parameter [26], it assumes a DMT-like force-displacement law and takes the asperity height distribution into account. Inputs to the GW model include the asperity radius of curvature, the asperity density and the asperity height distribution function. Each was independently assessed by two methods, and agreement was good. Further, the assumption of surface elasticity was validated. Quantitatively, however, the GW model with a Gaussian distribution function severely underestimated the measured trend for p/p_s<0.9. A possible reason was traced to convergence of the model at large values of d/σ_s. Using distribution functions with cutoff values, the experiment was more closely modeled. However, only an unreasonable cutoff value of d/σ_s=1.7 closely approximates the measured results. It was noted that the first model matches the experiment well if the asperity density is a free parameter. These results can be rationalized if the upper and lower surfaces are geometrically correlated, and this possibility should be explored in future work.

First order effects in the adhesion of rough surface under capillary conditions have been considered here. Many details deserve further attention. First, a surface layer of water exists on silicon according to the BET isotherm [46], but has not been taken into account. Second, the theory could be improved by better describing both the scale-dependent roughness as well as the free volume between the surfaces, perhaps according to a power spectrum description [47]. Third, the issues of how the menisci nucleate [48], how in detail menisci merge, and the rate at which the cracks heal at fixed p/p_s are of considerable interest.

Acknowledgments The author would like to thank Michael T. Dugger, who took the AFM images and independently measured the asperity radii. Patrick Klein and E. David Reedy made helpful comments on the manuscript. Sandia is a multiprogram laboratory operated by Sandia Corporation, a Lockheed Martin Company, for the United States Department of Energy's National Nuclear Security Administration under Contract DE-AC04-94AL85000.

Appendix: Calculation of Surface Height Change Due to Plasticity

As the crack tip passes over a given area, a moment-induced normal traction is applied. For a smooth surface, it can be shown [49, 50] that the average contact pressure over a zone of length t just beyond the crack tip P_{ct} is

$$P_{ct} = \frac{1.2}{\pi}\frac{Eht}{s^2} \tag{A-1}$$

over a region of length t. Through equation (2), the dependence of P_{ct} on adhesion can be calculated. For a rough surface, this pressure is localized to the highest asperities. The force on the highest asperity is initially $P_{ct}tw$, which is 160 μN for s=300 μm. As the crack tip passes over these asperities, they will experience a plastic deformation loading and unloading cycle. For a

spherical contact and assuming continuum plasticity (as may be applicable for a polycrystalline aggregate), the critical displacement for plastic deformation is [51]

$$\delta \geq \delta_c = \left(\frac{\pi(0.454 + 0.41\upsilon)H}{2E'}\right)^2 R \tag{A-2}$$

with $E' = E/2(1-\upsilon^2)$, δ_c=3.1 nm. The corresponding critical load is

$$P_c = \frac{4}{3}E'\sqrt{R\delta_c^3}. \tag{A-3}$$

Then P_c=10 μN. The elastic-plastic loading curve is [51]

$$P = 1.03P_c(\delta/\delta_c)^{1.425} \quad \text{for } 1 \leq (\delta/\delta_c) \leq 6. \tag{A-4}$$

while the residual plastic displacement is

$$\delta_{res} = \delta_{max}\left(1 - \frac{1}{(\delta_{max}/\delta_c)^{0.28}}\right)\left(1 - \frac{1}{(\delta_{max}/\delta_c)^{0.69}}\right) \tag{A-5}$$

where δ_{max} is the maximum displacement. Two other histograms similar to Fig. 11 were analyzed. In each, there are one or two outliers on the high end of the tail, similar to Fig. 11. As the crack tip passes over, let us assume there are two high asperities in the compressive region (of area *tw*) sharing the majority of the local load, say 50 μN each. (If the distribution is a continuous function, then this calculation overestimates δ_{res} because more asperities share the load.) Using equation (A-4), δ_{max}=9.3 nm. From equation (A-5), δ_{max}=3.0δ_c, and δ_{res}=(0.14) δ_{max}=1.3 nm. That is, the plastic deformation will shift the tail about 1.3 nm towards the center of the distribution.

References

1. Bocquet L, Charlaix E, Ciliberto S, Crassous J (1998) Moisture-induced ageing in granular media and the kinetics of capillary condensation. Nature 396:735.
2. Halsey TC, Levine AJ (1998) How sandcastles fall. Phys Rev Lett 80(14):3141.
3. Bachmann J, van der Ploeg RR (2002) A review on recent developments in soil retention theory: interfacial tension and temperature effects. J Plant Nutr Soil Sci 165:468.
4. Bentz D, Dale P (1995) Modelling drying shrinkage of cement paste and mortar. Part 1: structural models from nanometres to millimetres. Mater Constr 28(182):450–458.
5. Matthew Mate C (1992) Application of disjoining and capillary pressure to liquid lubricant films in magnetic recording. J Appl Phys 72(2):3084.
6. Mastrangelo CH, Hsu CH (1993) Mechanical stability and adhesion of microstructures under capillary forces—part I: basic theory. J Microelectromech Syst 2(1):33.
7. Mastrangelo CH, Hsu CH (1993) Mechanical stability and adhesion of microstructures under capillary forces—part II: experiments. J Microelectromech Syst 2(1):44.
8. Israelachvili J (1992) Intermolecular and surface forces. Academic, New York.
9. Stanley HM, Etsion I, Bogy DB (1990) Adhesion of contacting rough surfaces in the presence of sub-boundary lubrication. J Tribol Trans ASME 112(1):98.
10. Li Y, Talke FE (1992) A model for the effect of humidity on stiction of the head/disk interface. Tribol Trans 35(3):429.
11. Lawn BR (1993) Fracture of brittle solids, 2nd edn. Cambridge University Press, New York.
12. de Boer MP, Michalske TA (1999) Accurate method for determining adhesion of cantilever beams. J Appl Phys 86(2):817.
13. de Boer MP, Knapp JA, Michalske TA, Srinivasan U, Maboudian R (2000) Adhesion hysteresis of silane coated microcantilevers. Acta Mater 48(18–19):4531.
14. Knapp JA, de BoerMP (2002) Mechanics of microcantilever beams subject to combined electrostatic and adhesive forces. J Microelectromech Syst 11(6):754.
15. de Boer MP, Clews PJ, Smith BK, Michalske TA (1998) Adhesion of polysilicon microbeams in controlled humidity ambients. Mater. Res. Soc. Proc., vol. 518, In: Brown SB, Gilbert J, Guckel H, Howe RT, Johnson GC, Krulevitch P, Muhlstein CL (eds) San Francisco, CA, pp 131–136.
16. Sniegowski JJ, de Boer MP (2000) IC-compatible polysilicon surface micromachining. Annu Rev Mater Sci 30:297.
17. Kern W, Puotinen DA (1970) Cleaning solutions based on hydrogen peroxide for use in silicon semiconductor technology. RCA Rev 31(2):187.
18. Russick EM, Adkins CLJ, Dyck CW (1997) Supercritical carbon dioxide extraction of solvent from micromachined structures. In: Abraham MA, Sunol AK (eds) Supercritical fluids, extraction and pollution prevention; vol. 670. American Chemical Society, Washington, DC, pp 255–269.
19. Houston MR, Howe RT, Maboudian R (1997) Effect of hydrogen termination on the work of adhesion between rough polycrystalline silicon surfaces. J Appl Phys 81(8):3474.
20. Jensen BD, de Boer MP, Masters ND, Bitsie F, LaVan DA (2001) Interferometry of actuated cantilevers to determine material properties and test structure non-idealities in MEMS. J Microelectromech Syst 10(3):336.
21. DelRio FW, de Boer MP, Knapp JA, Reedy ED, Clews PJ, Dunn ML (2005) The role of van der Waals forces in adhesion of micromachined surfaces. Nat Mater 4(8):629–634.
22. Zheng Q, Durben DJ, Wolf GH, Angell CA (1991) Liquids at large negative pressures: water at the homgeneous nucleation limit. Science 254:829.
23. Fisher JC (1948) The fracture of liquids. J Appl Phys 19: 1062.
24. Douglas Frink LJ, van Swol F (1997) A molecular theory for surface forces adhesion measurements. J Chem Phys 106 (9):3782.
25. Christenson HK (1988) Adhesion between surface in undersaturated vapors—a reexamination of the influence of meniscus curvature and surface forces. J Coll Interface Sci 121 (1):170.
26. Fogden A, White LR (1990) Contact elasticity in the presence of capillary condensation. J Coll Inter Sci 138 (2):414.
27. Greenwood JA (1997) Adhesion of elastic spheres. Proc R Soc Lond A 453(1961):1277.

28. Johnson KL, Kendall K, Roberts AD (1971) Surface energy and the contact of elastic solids. Proc R Soc Lond A 324:301.
29. Derjaguin BV, Muller VM, Toporov YP (1975) Effect of contact deformations on the adhesion of particles. J Coll Inter Sci 53(2):314.
30. Sirghi L, Szoszkiewicz R, Riedo E (2006) Volume of a nanoscale bridge. Langmuir 22(3):1093.
31. Johnson KL (1985) Contact mechanics. Cambridge University Press, New York.
32. Greenwood JA, Williamson JBP (1966) Contact of nominally flat surfaces. Proc R Soc Lond A 295:300.
33. Greenwood JA, Tripp JH (1970–1971) The contact of two nominally flat rough surfaces. Proc Inst Mech Eng 185:625.
34. Fuller KNG, Tabor D (1975) The effect of surface roughness on the adhesion of elastic solids. Proc R Soc Lond A 345:327.
35. Maugis D (1996) On the contact and adhesion of rough surfaces. J Adhes Sci Technol 10(2):161.
36. McCool JI (1986) Comparison of models for the contact of rough surfaces. Wear 107:37.
37. Nayak PR (1971) Random process model of rough surfaces. J Lubr Technol 93:398.
38. Longuet-Higgins MS (1957) The statistical analysis of a random, moving surface. Philos Trans R Soc Lond A 249:321.
39. Pharr GM, Oliver WC, Clarke DR (1991) New evidence for a pressure-induced phase-transformation during the indentation of silicon. J Mater Res 6(6):1129.
40. Chang WR, Etsion I, Bogy DB (1987) An elastic-plastic model for the contact of rough surfaces. J Tribol Trans ASME 109:257.
41. Bora CK, Plesha ME, Flater EE, Street MD, Carpick RW, Redmond JM (2004) Multiscale roughness of MEMS surfaces. Proceedings of the ASME/STLE International Joint Tribology Conference, Long Beach, CA, pp. 133–139.
42. Yu N, Polycarpou AA (2002) Contact of rough surface with asymmetric distribution of asperity heights. Trans ASME J Tribol 124:367.
43. Kadin Y, Kligerman Y, Etsion I (2006) Unloading an elastic-plastic contact of rough surfaces. J Mech Phys Solids. (to be published)
44. Carpick RW, Flater EE, VanLangendon JR, de Boer MP (2002) Friction in MEMS: from single to multiple asperity contact. In: Society for experimental mechanics conference, Milwaukee, WI (June 10–12, 2002), pp 282–287.
45. Van Spengen WM, Puers R, De Wolf I (2002) A physical model to predict stiction in MEMS. J Micromechanics Microengineering 12:702.
46. Adamson AW (1990) Physical chemistry of surfaces. Wiley, New York.
47. Persson BNJ (2005) On the nature of surface roughness with application to contact mechanics, sealing, rubber friction and adhesion. J Phys Condens Matter 17(44):1071–1142.
48. Stroud WJ, Curry JE, Cushman JH (2001) Capillary condensation and snap-off in nanoscale contacts. Langmuir 17(3):688.
49. Wan K-T, Lawn BR, Horn RG (1992) Repulsive interaction between coplanar cracks in the double-cantilever geometrey. J Mater Res 7(6):1584.
50. DelRio FW, Dunn ML, Boyce BL, Corwin AD, de Boer MP (2005) The effect of nanoparticles on MEMS adhesion. J Appl Physi 99(10):104304-1-9.
51. Etsion I, Kligerman Y, Kadin Y (2005) Unloading of an elastic-plastic loaded spherical contact. Int J Solids Struct 42:3716.